



# Slide-free virtual histochemistry (Part II): detection of field cancerization

SIXIAN YOU,<sup>1,2</sup> YI SUN,<sup>1</sup> ERIC J. CHANEY,<sup>1</sup> YOUNG ZHAO,<sup>1</sup>  
JIANXIN CHEN,<sup>3,5</sup> STEPHEN A. BOPPART,<sup>1,2,4,6</sup> AND HAOHUA TU<sup>1,7</sup>

<sup>1</sup>Beckman Institute for Advanced Science and Technology, University of Illinois at Urbana-Champaign, Urbana, IL 61801, USA

<sup>2</sup>Department of Bioengineering, University of Illinois at Urbana-Champaign, Urbana, IL 61801, USA

<sup>3</sup>Fujian Provincial Key Laboratory for Photonics Technology, Key Laboratory of OptoElectronic Science and Technology for Medicine of Ministry of Education, Fujian Normal University, Fuzhou 350007, China

<sup>4</sup>Department of Electrical and Computer Engineering, Carle-Illinois College of Medicine, University of Illinois at Urbana-Champaign, Urbana, IL 61801, USA

<sup>5</sup>henjianxin@fjnu.edu.cn

<sup>6</sup>boppart@illinois.edu

<sup>7</sup>htu@illinois.edu

**Abstract:** Tumor-adjacent “normal” tissue constitutes a peri-tumoral field that affects early cancer detection, risk assessment, surgical decision, and postoperative surveillance. Modern genetic analysis has revealed valuable information from this field, but without the spatial resolution of optical microscopy to understand the vital microenvironments that surround individual cells. Rapidly advanced optical imaging techniques free of labor-intensive sample preparation, despite great promise to perform slide-free imaging of cell *structure* and shift the histology-centered cancer diagnostic paradigm, have lacked compatible and complementary histochemical imaging of cell *function* or *phenotype* to interrogate the peri-tumoral field. In the first part (Part I) of this two-part series study, we developed a technique of slide-free virtual histochemistry to phenotype various cells in *in vivo* animal and *ex vivo* human tissue. Here, in the second part (Part II) of this two-part series study, we employ this technique to examine various peri-tumoral fields and produce the volumetric histochemical evidence of field cancerization consistent with the structural changes at larger spatial scales. We also link the field cancerization with cancer dormancy in a significant portion of breast cancer patients.

© 2018 Optical Society of America under the terms of the [OSA Open Access Publishing Agreement](#)

## 1. Introduction

Standard hematoxylin-and-eosin histology (H&E) and subsequent immunohistochemistry (IHC) in preoperative diagnosis of small biopsies and postoperative prognosis or surveillance of tissue samples, along with fast frozen section analysis (FSA) of surgical specimens during intraoperative assessment, form the gold standard for cancer diagnostic management that has not undergone a paradigmatic shift since 1950s. Recently, a wave of novel optical imaging technologies have emerged as volumetric alternatives [1–6] (Table 1) to typically two-dimensional-based H&E and FSA, and have been used to directly visualize fresh or formalin-fixed tissue in a digital form without labor-intensive (and artifact-prone) sample preparation on an H&E (or FSA) microscope slide [7]. The digital image data can be converted into virtual H&E images understandable by pathologists, which structurally highlight cell nuclei from the cytoplasm and the extracellular matrix as if the images were acquired by standard H&E [1–4]. The resulting slide-free virtual H&E imaging (SF-vH&E) appears non-perturbative to the sample, even with external fluorescent labeling [1,3], and may thus conserve the valuable tissue specimen as a resource for subsequent molecular/genetic analysis and future use [2]. Additional advantages associated with volumetric imaging [7] and label-

free intraoperative imaging *in situ* (*in vivo* inside the surgical cavity without removing the tissue) [8] reinforce the view that this paradigmatic shift is emergent [9].

However, remaining obstacles in both the non-intraoperative (preoperative or postoperative) assessment and intraoperative assessment must be overcome to enable a full paradigmatic shift. Outside of the intraoperative setting, imaging techniques for slide-free stain-free functional/metabolic assessment are currently lacking. Without this imaging, the usefulness of SF-vH&E would be considerably limited, e.g., to fast but rudimentary cancer diagnosis or determining adequacy of biopsy sampling [1]. If conventional IHC or tissue-clearing-assisted volumetric IHC imaging [10] (Table 1) is required to follow SF-vH&E, the exact limitation of histology (labor-intensive sample/slide preparation) that SF-vH&E has avoided would be largely retained. In the intraoperative assessment, the benefit to replace FSA with faster SF-vH&E is compromised by a lack of information about the peri-tumoral field with field cancerization [11–14], which may define surgical tumor margins differently from sporadic tumorigenesis. Specifically, a negative surgical margin validated by either FSA or SF-vH&E may not prevent the local recurrence of a second field tumor in an unresected cancerized field [12]. Although it is possible to detect field cancerization in a peri-tumoral field by SF-vH&E, just like Slaughter and associates did in 1953 by H&E [11], the associated interobserver variability to discern subtle precancerous morphologies (hyperplasia, metaplasia, dysplasia, etc.) has fundamentally limited this practice [13,14]. There is a need for a quantitative imaging technique that could objectively assess the metabolic and structural properties of the complex microenvironment.

It is then clear that in order to enable a full paradigmatic shift, a slide-free histochemical imaging technique free of labor-intensive sample preparation is needed to phenotype not only the primary tumor cells or tumor-associated cells for prognosis, but also other cells in the surrounding peri-tumoral field for detecting field cancerization. The definition (detection) of field cancerization by cell phenotypical changes has gained recognition over the more conventional definition (detection) by cell genetic or epigenetic alterations, due to the challenge to distinguish cancerized lineages against abundant mutant lineages [14]. Also, volumetric imaging is preferred to obtain spatial information, which is absent from genetic analysis, to discern cell niches, vasculature, and layer/duct formations [10].

In the first part (Part I) [15] of this two-part series study, we demonstrated a technique of label-free tetra-modal multiphoton microscopy for slide-free volumetric histochemical imaging (i.e. slide-free virtual histochemistry) compatible with label-free SF-vH&E (Table 1). This technique has no labeling-associated disadvantages [9], and can in principle realize *in situ* intraoperative imaging [8]. Here, in the second part (Part II) of this two-part series study, we demonstrate the diagnostic value of this technique in breast cancer not only for the primary tumor but also for the peri-tumoral field that has not routinely provided imaging-based diagnostic value previously.

Table 1. Representative slide-free imaging modalities for histology.

Technological platform	UV microscopy (MUSE)	Light-sheet microscopy -1	Dual-modal multiphoton microscopy	3	Stimulated Raman microscopy	4	5	Photoacoustic microscopy	6	Optical coherence tomography	Light-sheet microscopy -2	Tetra-modal multiphoton microscopy
Reference	1	2	3	4	5	6	10					This study
Nature	virtual H&E histology	virtual H&E histology	virtual H&E histology	virtual H&E histology	virtual H&E-like histology	virtual H&E-like histology	immuno-histochemistry	virtual H&E-like histology	immuno-histochemistry	histochemistry	immuno-histochemistry	virtual histochemistry
Tissue sample	fresh, formalin-fixed	fresh, formalin-fixed	fresh, formalin-fixed	fresh	fresh	fresh	fresh	fresh	fresh	fresh	paraffin-embedded	fresh
Tissue treatment	no	occasional clearing	no	no	no	no	no	no	no	no	clearing required	no
Labeling	yes	yes	yes	no	no	no	no	no	no	no	yes	no
Imaging contrast	fluorescence	fluorescence	fluorescence, SHG	fluorescence, SHG	fluorescence, SHG	fluorescence, SHG	fluorescence, SHG	absorption	scattering	fluorescence	fluorescence	fluorescence, SHG, THG
Dimension of imaging	2.5	3	3	3	3	3	3	3	3	3	3	3
# of contrasts in one scan	2	2	2	1	1	1	1	1	1	1	2	4
# of scans for one image	1	1	1	2	1	1	1	1	1	1	1	1
Nucleus contrast generation	Hoechst, DAPI	DRAQ5, acridine orange	acridine orange	differentiated vibration strength	nuclear UV absorption	UV absorption	YO-PRO	nuclear UV absorption	unclear	unclear	YO-PRO	endogenous fluorescence
Counter-nucleus contrast	Rhodamine	eosin	SHG	nonspecific	(absent)	unclear	diverse antibodies	(absent)	unclear	unclear	diverse antibodies	endogenous fluorescence, THG
Collagen contrast	nonspecific	nonspecific	SHG	nonspecific	nonspecific	unclear	specific antibody	nonspecific	unclear	unclear	specific antibody	SHG
Signal detection	epi	epi-like	epi	transmission	transmission, epi	transmission, epi	epi-like	transmission, epi	epi	epi	epi-like	epi
Optical source	UV light-emitting diode	visible fiber-coupled laser	ultrafast solid-state laser	engineered fiber laser	tunable solid-state laser	halogen bulb	visible fiber-coupled laser	tunable solid-state laser	halogen bulb	halogen bulb	visible fiber-coupled laser	engineered fiber laser
Demonstrated features or applications	general H&E histology free of microscope slide	general H&E histology free of microscope slide	breast cancer margin assessment	brain cancer intraoperative margin assessment	breast cancer intraoperative margin assessment	breast cancer <i>ex vivo</i> pathology	general volumetric immuno-histochemistry	breast cancer intraoperative margin assessment	breast cancer <i>ex vivo</i> pathology	breast cancer <i>ex vivo</i> pathology	general volumetric immuno-histochemistry	breast cancer peri-tumoral field interrogation

## 2. Methods

The details of the laser source, multiphoton microscope, and biological materials have been provided in Part I of this study [15]. Fresh human breast tissue samples were imaged immediately after surgery. Tissue was stored in a cool saline solution at a temperature of 2–8 °C before imaging. Cancerous breast tissue samples were obtained from female subjects undergoing mastectomy and diagnosed by a board-certified pathologist as having invasive ductal carcinoma. Peri-tumoral normal appearing tissue specimens were acquired 1–10 cm beyond the perceived primary tumor boundary. Normal breast tissue samples were obtained from female subjects undergoing breast reduction surgery, with no history of cancer. For each (frequently large) peri-tumoral normal appearing tissue specimen from a patient, small specimens ~0.5 cm in size were dissected for multiphoton imaging (Fig. 1). Small portions of matched tumor specimens, containing both primary tumor and non-tumor tissue bordering the tumor within 1 cm (tumor center along with vicinity of the tumor boundary), were available from the patients and similarly imaged (Fig. 1). The distance of 1 cm was chosen to delineate the boundary between the tumor-adjacent normal tissue and the potentially cancerous tissue based on the experience of the board-certified pathologists at Carle Foundation Hospital. The full field-of-view for stain-free imaging ranges from 1 to 4 mm<sup>2</sup> depending on the size and geometry of the tissue. A set of customized color maps was used for this imaging study, namely magenta for THG, cyan for 3PAF/NADH, green for SHG, and yellow for 2PAF/FAD. Strong signals from the autofluorescence channels can be attributed to the high concentration of the auto-fluorophores within the excitation volume. Strong signals from THG can be attributed to the local change in the optical heterogeneity, e.g. lipid-water interface. In parallel to the multiphoton imaging, postoperative H&E histology was performed on all tumor specimens and complemented the preoperative diagnosis by biopsies.

Standard H&E histology was performed on some rat tissue specimens, and some structures in the histology images were correlated with similar structures in the multiphoton images. Although best effort was taken to find the exact sites of multiphoton imaging, the structural distortion and component loss due to histological sample treatments hindered more precise and comprehensive correlation between the standard histology and our tetra-modal imaging on the micron scale.

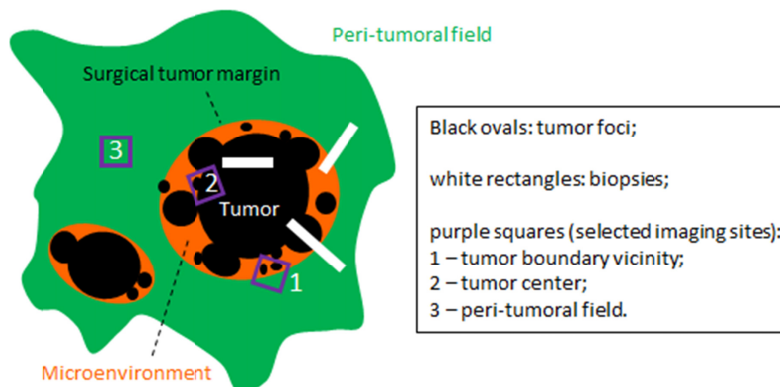


Fig. 1. Selective biopsy and imaging of a specimen with field cancerization.

## 3. Results

### 3.1 Phenotyping cancer-associated epithelial and endothelial cells

Optical phenotyping of various non-epithelial cells has been discussed in Part I of this study, and should also be applicable to epithelial cells widely observed in histology (Figs. 2(a), 2(b)), considering its ability to differentiate yellow-colored stromal cells from cyan- and magenta-colored cancer-associated stromal cells present in one small field of view

(arrowheads; Fig. 3(i)). To phenotype the luminal epithelial cells in mammary ducts, we conducted extensive imaging of control rats ( $n = 10$ ) and did detect mammary duct-like structures (arrowheads, Figs. 3(g), 3(h)). Although cyan-color pixels can be observed at the periphery of the duct in Fig. 3(g), no endothelial-cell structures were revealed in the normal mammary tissue. Interestingly, these epithelial cells might emerge in cancer-associated specimens as having cyan-colored nuclei (arrowheads, Figs. 3(b), 3(c)) similar to matched primary tumor cells (Fig. 3(a)), which were validated by H&E histology (Figs. 2(c), 2(d)). As mentioned in Part I of this study [15], the endothelial cells were recognized by their unique elongated shape as well as their context in which they are aligned well along the direction of the vessel, which highly correlates with their typical histologic morphology. The different optical signatures could be attributed to their active metabolic status. Endothelial cells with cyan outlines indicate high NADH concentration, which is associated with glycolysis as well as hypoxia. Endothelial cells with strong THG signals indicated the local presence of water around the cells.

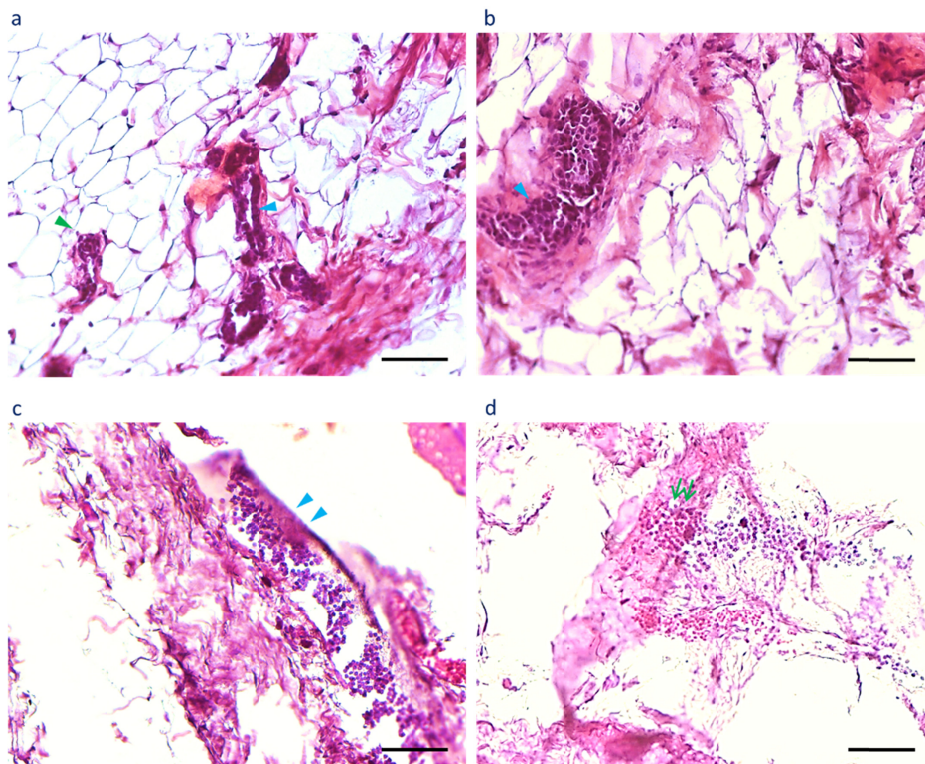


Fig. 2. Standard H&E histology of mammary tissue in a control rat and a carcinogen-induced rat. (a) H&E image of control mammary tissue reveals normal mammary ducts (cyan arrowhead) and alveoli (green arrowhead) lined with luminal epithelial cells. (b) H&E image of the same mammary tissue in a different field-of-view reveals a normal mammary duct filled with luminal epithelial cells (cyan arrowhead). (c) H&E image of the peri-tumoral field reveals a precancerous mammary duct (cyan arrowheads). (d) H&E image of the same tumor-adjacent mammary tissue in a different field-of-view reveals the coupling between a branched mammary duct and a blood vessel (green double-arrow). Scale bars: 100  $\mu\text{m}$ .

This illumination of otherwise invisible ductal epithelial cells reflects their underlying phenotypical or metabolic changes toward neo-progression (Table 2, Row 3). More studies are clearly needed to prove that these features can be used as biomarkers for carcinogenesis. We identified normal ductal epithelial cells as largely yellow-colored cytoplasmic fragments in control specimens (arrowheads, Figs. 3(l), 3(m)), which could turn into a magenta-colored

cancer-associated phenotype in peri-tumoral fields (arrowhead, Fig. 3(r)) and tumor regions (arrowhead, Fig. 3(q)) similar to matched primary tumor cells (Fig. 3(p)).

Endothelial cells are observed as elongated cyan-colored cells in Part I of this study [15], but are not observable in developed blood vessels with yellow-colored erythrocytes (Figs. 3(i), 3(j), 3(n), 3(o)). However, in the cancer-associated rat (or human) blood vessels, endothelial cells with elongated cyan-colored nuclei (or a magenta-colored cell cytoplasm) emerge as developing blood vessels (or capillaries) [Fig. 3(d) (or Fig. 3(s))] (Table 2), and develop into matured blood vessels (or connect with larger magenta-colored developing blood vessels) [Fig. 3(e) (or Fig. 3(t))].

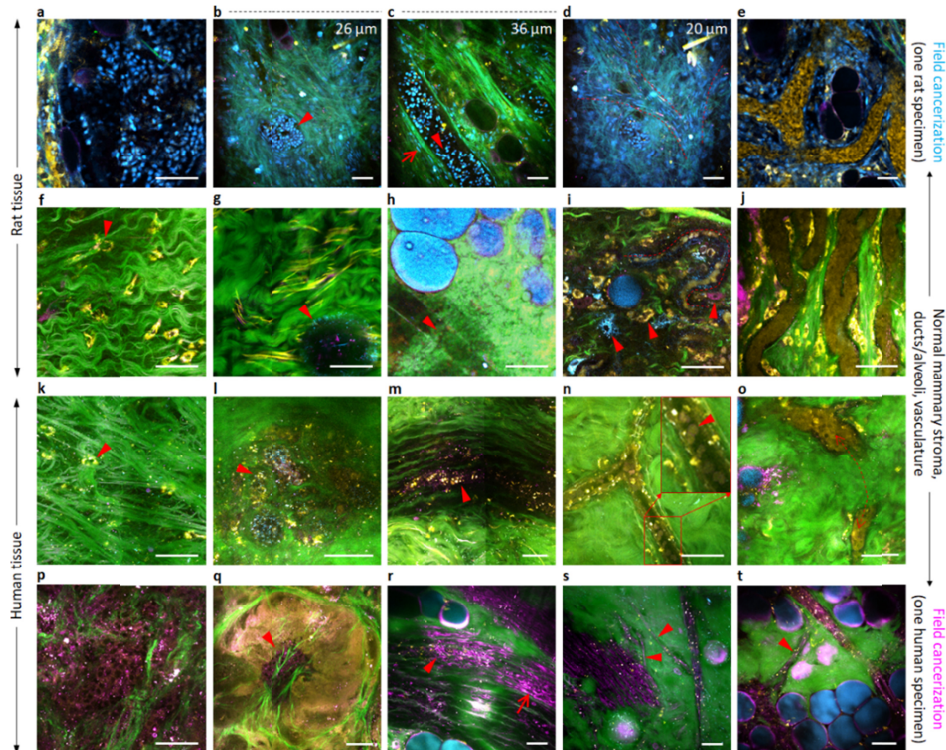


Fig. 3. Phenotypical changes of rat mammary and human breast cells in cyan- and magenta-colored field cancerization, respectively. (a) Rat primary tumor cells with cyan-colored nuclei. (b) Rat epithelial cells in a mammary alveolus with cyan-colored nuclei. (c) Rat epithelial cells in a mammary duct with cyan-colored nuclei. (d) Rat endothelial cells of developing blood vessels with elongated cyan-colored nuclei. (e) Similar rat cells that line developed blood vessels. (f) Rat stromal cells in remote peri-tumoral field. (g) Normal rat mammary duct (cross-sectional view) lacking visible epithelial cells. (h) Normal rat mammary duct (lateral view) lacking visible epithelial cells. (i) Developing rat neo-vasculature (broken line) lacking visible endothelial cells. (j) Developed rat blood vessel lacking visible endothelial cells. (k) Human stromal cells in remote peri-tumoral field. (l) Normal human mammary duct (cross-sectional view) with yellow-magenta-colored epithelial cells. (m) Normal human mammary duct (lateral view) with yellow-magenta-colored epithelial cells. (n) Developing human blood vessel lacking visible endothelial cells. (o) Developed human blood vessel lacking visible endothelial cells. (p) Human primary tumor cells with a magenta-colored cytoplasm. (q) Human epithelial cells in a tumor region with a magenta-colored cytoplasm ([Visualization 1](#)). (s) Human endothelial cells of developing blood capillaries with a magenta-colored cell body. (t) Connection of a magenta-colored blood capillary (broken box) with a larger magenta-colored developing blood vessel ([Visualization 2](#)). Images (b), (c), and (d) are from different depths of one field-of-view. Scale bars: 50  $\mu\text{m}$ .

Table 2. Classified vital cells in mammary tissue with distinct optical phenotypes.

Cell type	Yellow cytoplasm	Yellow nucleus	Cyan cytoplasm	Cyan nucleus	Magenta cytoplasm	Magenta nucleus	Cell shape
<i>Rat and human normal cells</i>							
Fibroblast	1	0	0	0	0	0	spindle
Adipocyte	1	0	0	0	0	0	crescent
Erythrocyte	1	0	0	0	0-1	0	round
Immune cell 1	1	0	0	0	1	0	round-like
Yellow-colored stromal cell	1	0	0	0	0	0	amoeboid
<i>Rat and human cancer-associated cells</i>							
Tumor cells	0-1	0-1	0-1	0-1	0-1	0-1	diverse
Magenta-colored stromal cell	0	0	0	0	1	0	amoeboid
Cyan-colored stromal cell	0	0	1	0	0	0	amoeboid
<i>Rat cells specific to cyan-colored field cancerization (2 out of 16 carcinogen-injected rats)</i>							
Tumor cell	0	0-1	0	1	0	0	round-like
Mesenchymal cell	0	0	0	1	0	0	elongated
Endothelial cell	0	0	0	1	0	0	elongated
Luminal epithelial	0	0	0	1	0	0	round-like
<i>Human cells specific to magenta-colored field cancerization (4 out of 12 breast cancer patients)</i>							
Tumor cell	0-1	0	0	0	1	0	round-like
Endothelial cell	0	0	0	0	1	0	elongated
Luminal epithelial	0	0	0	0	1	0	
Myoepithelial	0	0	0	0	1	0	elongated

### 3.2 Detecting field cancerization in the peri-tumoral field

In our breast cancer rat model, we frequently observed macroscopic (~1 cm) multifocal tumors by gross examination. A natural question arises whether grossly invisible microscopic (<1 mm) tumor foci, often termed as lesions, patches, and clusters, occur independently as the result of field cancerization [12–14]. According to the classical paper by Slaughter and associates [11], field cancerization in breast cancer can be characterized by three unique structures (Fig. 1): (i) emergence of both macroscopic and microscopic tumor foci in a field of precancerous tissue with abnormality of hyperplasia, metaplasia, or dysplasia; (ii) growth of multiple separate (independent) microscopic foci of DCIS and/or invasive breast cancer (IBC) near grossly visible tumor boundary or surgical margin; and (iii) coalescence of multiple (contiguous) tumor foci at the tumor center.

To answer this question, we identified a carcinogen-injected rat with macroscopic multifocal tumors, and performed wide-field (~2 mm<sup>2</sup> with stitched adjacent high-resolution field-of-views collected by scanning the specimen with a mechanical stage) tetra-modal imaging on one of them near a grossly detected tumor boundary (Fig. 4(a)), at the tumor center (Fig. 4(b)), and in the more remote peri-tumoral field (Fig. 4(c)). Noticeably, two separate egg-shaped microscopic (~300 μm) tumor foci emerge in one field of view, with similar tumor cells visible by their cyan-colored nuclei (Fig. 4(a)). Also, similar cyan-colored nuclei are found inside several mammary ducts in the adjacent peri-tumoral field (arrowheads, Fig. 4(a)), revealing the cancer-associated rat mammary epithelium (Fig. 3(c) vs. Fig. 3(h)) that appears normal or precancerous (hyperplasia, metaplasia, or dysplasia) by H&E histology (Fig. 4(a), inset) but could have suffered genetic alterations [17]. Moreover, the imaging site near the tumor center exhibits the apparent coalescence of two larger (~1 mm) tumor foci (Fig. 4(b)). Thus, all three unique structures of field cancerization are present and imaged in this rat tumor.

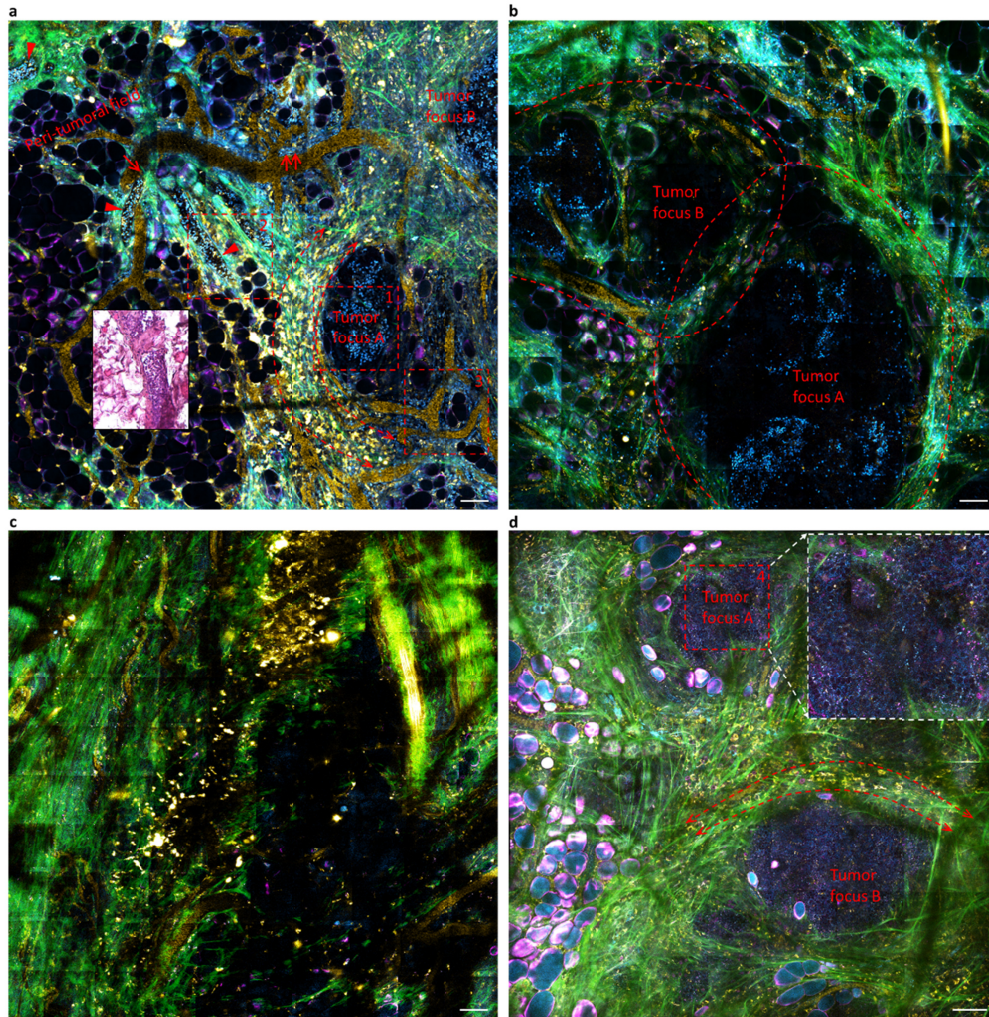


Fig. 4. Wide-field tetra-modal imaging of cyan-colored field cancerization in carcinogen-inject rats. Images (a), (b), and (c) reflect the vicinity of mammary tumor boundary, tumor center, and the remote peri-tumoral field of a tumor in one rat, respectively, while image (d) reflects the vicinity of the tumor boundary in another rat for direct comparison with (a). Epithelial cells (arrowheads), endothelial cells lining yellow-colored blood vessels (double arrows), and numerous stromal cells in the peri-tumoral field share the same optical phenotype of cyan-colored nuclei with the primary tumor cells (broken box 1), illuminating a cyan-colored field cancerization beyond the primary tumor(s). Dashed boxes 1, 2, and 3 are also plotted in Figs. 3(a), 3(b)-3(d), and 3(e), respectively. Scale bars: 100  $\mu$ m.

Although this field cancerization could be alternatively detected by H&E histology or SF-vH&E structural imaging, our tetra-modal histochemical imaging offers another relatively independent and perhaps more elegant way to detect the field cancerization (Figs. 4(a)-4(c)), using the unique common optical phenotype of cyan-colored nuclei that simultaneously dominates the constituent cells of the tumor foci (Fig. 3(a), corresponding to broken box 1 in Fig. 4(a)), the epithelia (Figs. 3(b), 3(c), corresponding to broken box 2 in Fig. 4(a)), the vasculature (Figs. 3(d), 3(e), corresponding to broken boxes 2 and 3 in Fig. 4(a), respectively), and the vasculature-free stroma. The resulting cyan-colored field cancerization appears to be a highly abnormal event (Figs. 3(a)-3(e) vs. Figures 3(f)-3(j)), considering the heterogeneity of these tissue components with widely variable colors (Fig. 3). For example,

another carcinogen-injected rat exhibits a similar tumor microenvironment and peri-tumoral field (Fig. 4(d)), but no cyan-colored field cancerization is present to expand the corresponding phenotype of tumor cells with cyan-colored cytoplasm (box 4, Fig. 4(d)). This phenotype of tumor cells reproduces that of the reported tumor cells in a transgenic mouse breast cancer model [18]. Interestingly, all observed tumor foci are surrounded by a similar microenvironment of neo-vasculature, cancer-associated collagen structure, and infiltrating FAD-rich NADH-poor (i.e., yellow-colored) macrophages [18] (bidirectional arrows, Figs. 4(a), 4(d)), independent of the breast cancer model selected and the presence of field cancerization.

To seek clinical relevance of field cancerization in a subject with multifocal tumors, we performed the tetra-modal imaging on one 2.1-cm sized tumor near a grossly visible tumor boundary (Fig. 5(a)), at a site 2-5 cm away from this boundary (Fig. 5(b)), and in the more remote peri-tumoral field >5 cm away from the boundary (Figs. 5(c), 5(d)). This tumor exhibits a magenta-colored field cancerization of tumor foci (broken box and ovals, Fig. 5(b)), epithelia (arrow, Fig. 5(a)), vasculature (arrowheads, Fig. 5(a)), and vasculature-free stroma that strikingly echoes the cyan-colored field cancerization in the rat tumors (Figs. 3(a)-3(e) vs. Figures 3(p)-3(t)). In particular, the volumetric imaging of a mammary duct reveals luminal epithelial cells (arrowhead, Fig. 3(r)) enclosed by elongated myoepithelial cells (arrow, Fig. 3(r)) [19] ([Visualization 1](#)), and the connection of a blood capillary (arrowhead, Fig. 3(t)) to a larger blood vessel ([Visualization 2](#)). The cyan- or magenta-colored field cancerization fades away in the remote peri-tumoral fields (Figs. 4(c), 5(c)) that contain normal mammary ducts (Fig. 5(d)), suggesting the presence of a new molecular/metabolic margin that is outside of the conventional H&E-defined margin in the cancerized field [12–14].

From the perspective of this colored field cancerization, our rat mammary tumor model recapitulates human breast cancer development, with no interference from xenografting, implantation, immune suppression, genetic modification, or fluorescence protein expression.

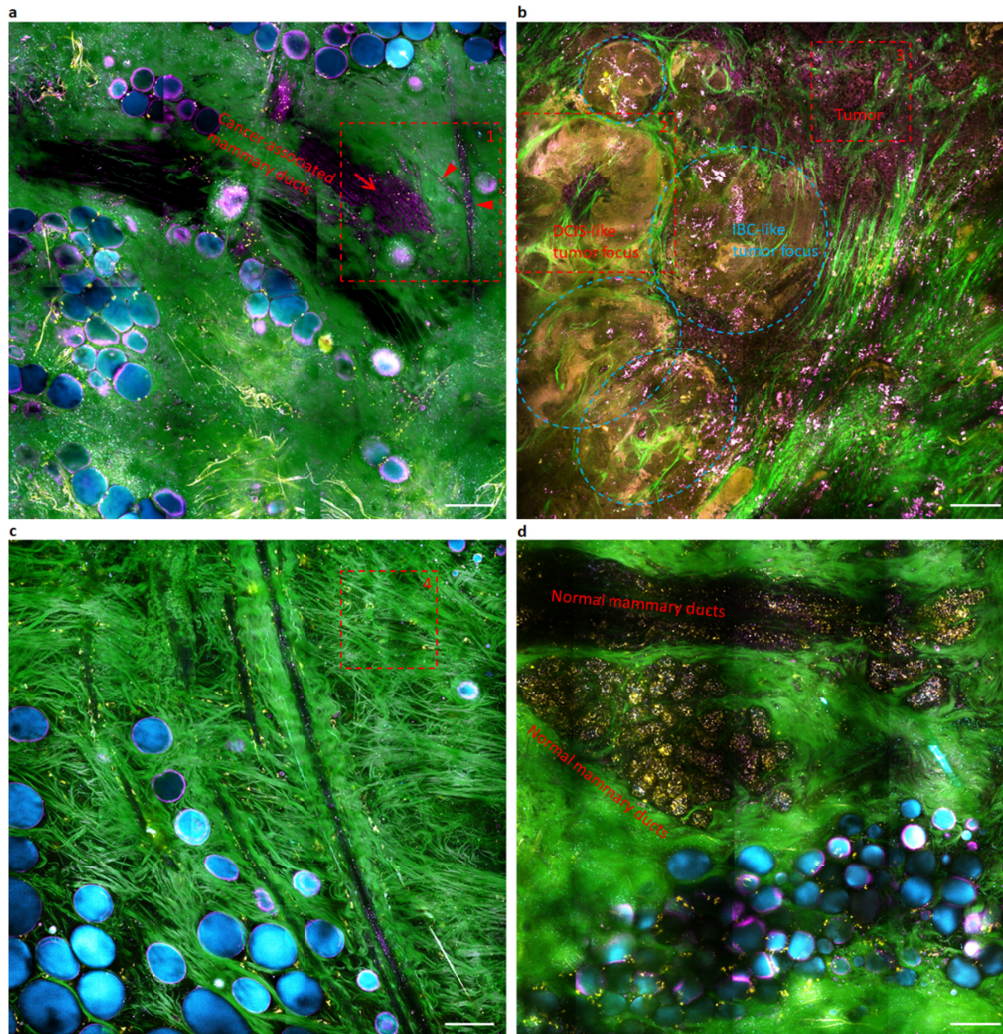


Fig. 5. Wide-field tetra-modal imaging of magenta-colored field cancerization in a cancer patient (Subject #388). Images (a), (b), and (c-d) reflect the vicinity of breast tumor boundary, tumor center, and the remote peri-tumoral fields of a tumor, respectively. Epithelial cells (arrow) and endothelial cells lining blood vessels (arrowheads) share the same optical phenotype of magenta-colored cytoplasm (or cell body) with the primary tumor cells (broken box 3), illuminating a magenta-colored field cancerization beyond the primary tumor(s). Dashed boxes 1, 2, 3, and 4 are also plotted in Figs. 3(s), 3(q), 3(p), and 3(k), respectively. Scale bars: 100  $\mu\text{m}$ .

By selective wide-field tissue imaging that includes the peri-tumoral field, in a manner analogous to breast cancer sampling with multiple (4-8) core-needle biopsies (Fig. 1) for diagnosis, we observed the same magenta-colored field cancerization in 4 of 12 cancer patients. This field cancerization demonstrates potential to serve as a new biomarker [20] to stratify breast cancer patients into two groups (Table 3). The negative patient group ( $n = 8$ ) largely shares with the control group ( $n = 8$ ) similar normal mammary ducts (Figs. 3(l), 3(m)), blood vessels (Figs. 3(n), 3(o)), and vasculature-free stroma (Fig. 3(k)), without magenta-colored constituent epithelial cells, endothelial cells, and stromal cells, respectively. The different optical field characteristics in rat versus human tumor tissue can likely be attributed to molecular differences between the pre-clinical rat model and the human tumor tissue. This is an important finding that highlights the differences between this commonly-used pre-

clinical model and humans, but future studies are needed to elucidate exactly what molecular differences exist.

**Table 3. Stratification of breast cancer patients by magenta-colored field cancerization.**

#	Field cancerization	Age at surgery	Detection /diagnosis	TNM stage	Pathology
359	+	40	Symptom; self-detected	pT2; pN1a	Invasive ductal carcinoma grade 2; Her2-;
393	+	48	Symptom; palpable mass	pT0; pN0	Atypical ductal hyperplasia; BRCA 1+; confirmed case of multifocal tumors
388	+	46	Symptom; self-detected	pT2; pN2a	Invasive ductal carcinoma grade 1; multifocal; ER+, PR+, Her2+; confirmed case of multifocal tumors
401	+	71	Self-detected; history of DCIS	pT2; pN1a	Invasive carcinoma grade 2;
372	-	82	Self-detected; history of DCIS	pT1c; pN0	Invasive papillary carcinoma grade 2; previous lumpectomy
373	-	59	Radiology	pT3; pN2a	Invasive ductal carcinoma grade 3;
375	-	76	Radiology	pT1c; pN1a	Invasive papillary carcinoma grade 3; ER+; PR+; recurrent cancer
371	-	65	Radiology	pT1c; pN0	Invasive ductal carcinoma grade 1; ER+, PR+, Her2-;
394	-	56	Radiology	pT1c; pN1a	Invasive ductal carcinoma grade 1; BRCA+;
398	-	37	Physician detected	pT1c; pN0	Invasive carcinoma grade 2;
400	-	75	Self-detected	pT1c; pN1a	Invasive ductal carcinoma grade 2; Her2-;
402	-	76	Radiology	pT1c; pN0	Invasive ductal carcinoma grade 2; multifocal; Her2-;

### 3.3 Observing signatures of cancer dormancy

In the cyan-colored field cancerization, one H&E-benign (normal or precancerous) but histochemically cancerous rat mammary duct clearly intertwines with surrounding cancer-associated blood vessels at a cooperative juncture (arrow, Fig. 4(a)), allowing possible intravasation of the epithelial cells with cyan-colored nuclei into systemic blood circulation. Because the corresponding peri-tumoral field approximates a precancerous field before (or after) the emergence (or resection) of the primary tumor, this intravasation may function as the early dissemination of precancerous (dormant tumor) cells [21] during cancer dormancy [22] that dominates overt metastasis (cancer mortality) [23]. It is thus important to investigate whether the observed field cancerization possesses the three characteristic signatures of this cancer dormancy [21–23]: (i) dormant tumor cells are stem-like cells resistant to therapy that targets primary tumor cells; (ii) early dissemination of the dormant tumor cells requires a hijacked program of branched mammary tubulogenesis; and (iii) therapeutic suppression (natural progression) of tumor proliferation rejuvenates (impedes) this early dissemination.

There is strong evidence that indicates this stem-like origin of the cyan-colored field cancerization. First, the dominant optical phenotype of cyan-colored nuclei corresponds to concentrated unbound nuclear NADH that has been associated with progenitor (stem-like) cells [24]. Second, the observed alveoli/ducts in the peri-tumoral field remarkably resemble the mammary gland tubulogenesis by normal stem cells [25] (Figs. 3(b)-3(d) vs. Figure 1 in ref. 25). Third, stem-like gene signatures have been associated with the early dissemination of low-burden cancerous tissue that approximates a precancerous/dormant peri-tumoral field [26]. This plausible stem-like origin suggests that the dominant optical phenotype (cyan-colored nuclei) might originate from one stem cell progenitor, which passed this optical phenotype and the underlying genotype to all its differentiated descendants of epithelial cells, endothelial cells, stromal cells, and tumor cells that share the optical phenotype (monoclonal tumor expansion) [12]. The magenta-colored field cancerization observed in the human

tumors might originate from stem cell progenitors with a magenta-colored optical phenotype. Further investigations will be performed in the future to systematically establish the link between the optical phenotypes and different cell types. Regardless of the color (dominant optical phenotype) of field cancerization, a common stem-like origin may link it with cancer dormancy.

To critically test this plausible link to cancer dormancy, we recognize the recently observed reversible transition between binary states of tumor cell proliferation vs. dissemination in breast cancer [23]. According to this transition, preoperative suppression of the proliferation by chemotherapy rejuvenates the early dissemination, and would enhance (suppress) the magenta-colored field cancerization if such link does (not) exist. We thus performed imaging of an *ex vivo* specimen from a cancer patient after preoperative neoadjuvant chemotherapy followed by mastectomy. The specimen was dissected from the grossly normal tissue between two multifocal primary tumors (diagnosed by core-needle biopsy) separated by ~5 cm. The two tumors were 1.1-cm and 0.3-cm in size on x-ray mammography, but underwent a pathologic complete response after chemotherapy [27] (no tumor mass was grossly found or histologically identified around the coiled biopsy marker clip). In contrast to this seemingly favorable prognosis by H&E histology, our tetra-modal imaging of the specimen in the peri-tumoral field pointed to a rather different picture (Fig. 6(a)). The chemotherapy seemed to activate branched mammary tubulogenesis [21,23] (Fig. 6(b); [Visualization 3](#)) in comparison to its counterpart without preoperative therapy ([Visualization 1](#)). This mammary tubulogenesis was intertwined with irregular blood capillaries for plausible dissemination (Fig. 6(b)). One capillary was undergoing active development by assembling intracellular vacuoles of single endothelial cells [28] (arrowhead, Fig. 6(c)), while the connecting larger blood vessel was undergoing active sprouting development (Fig. 6(c); [Visualization 4](#)) in comparison to its therapy-free counterpart ([Visualization 2](#)). This enhanced picture of magenta-colored field cancerization (Fig. 6) over its therapy-free counterpart (Fig. 5(a)) indirectly validates the above three characteristic signatures, and thus supports the link between field cancerization and cancer dormancy.

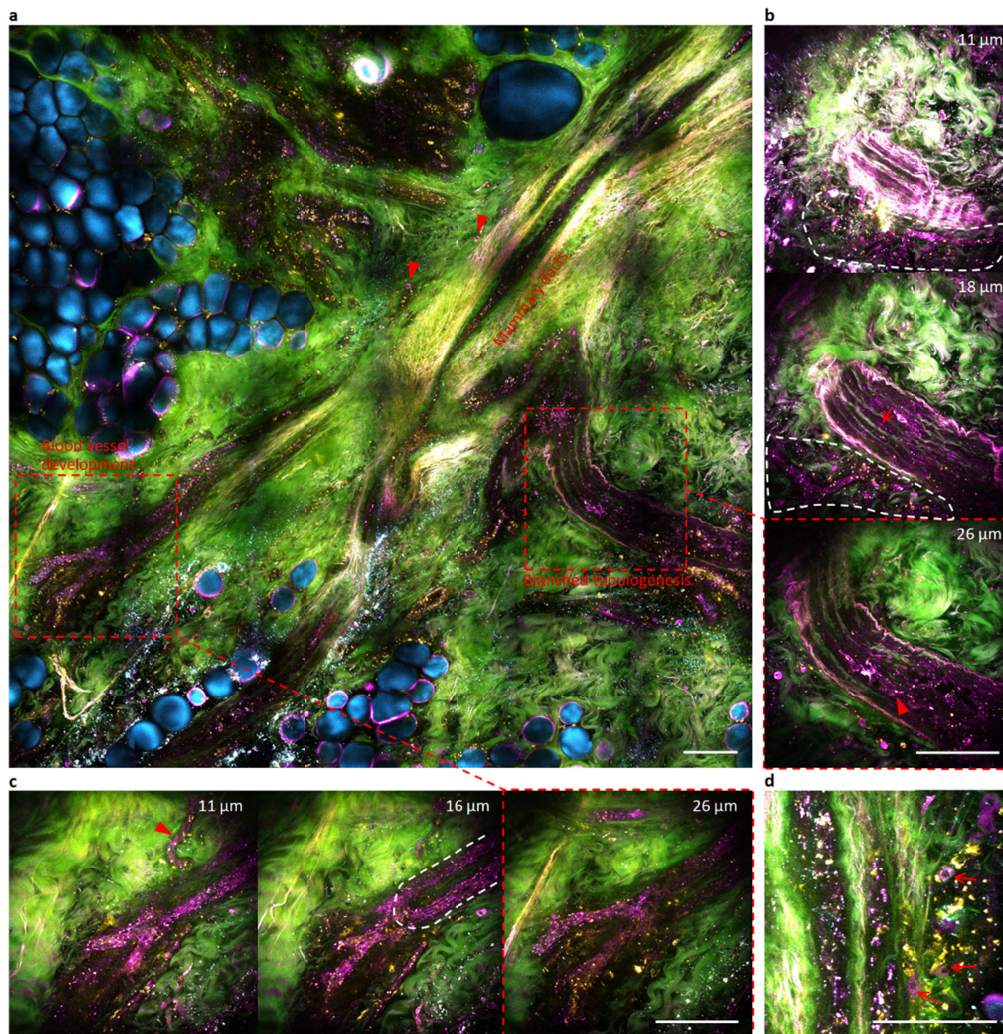


Fig. 6. Wide-field and selective volumetric tetra-modal imaging of rejuvenated magenta-colored field cancerization by chemotherapeutically eliminating multifocal primary tumors in a cancer patient (Subject #393). (a) Wide-field tetra-modal image of the peri-tumoral field with root-like mammary ducts, with two regions of interest subjective to selective volumetric tetra-modal imaging (broken boxes). (b) Selective volumetric tetra-modal images at three depths showing branched mammary tubulogenesis with luminal epithelial cells (arrowhead) and myoepithelial cells (arrow), which intertwines with developing capillaries surrounded by magenta-colored stromal cells (region of white broken curve) (Visualization 3). (c) Selective volumetric tetra-modal images at three depths showing blood vessel development of a capillary (arrowhead) and a connected sprouting vessel (region of white broken curve) (Visualization 4). (d) main branch of mammary ducts with peripheral magenta-colored stromal cells (arrows) different from yellow-colored stromal cells. Scale bars: 100  $\mu\text{m}$ .

#### 4. Discussion

Field cancerization is a paradigm for tumorigenesis and is ubiquitous in aged human organs. The emergence of multifocal primary tumors from a cancerized field is fundamentally different from sporadic tumorigenesis without this field, and calls for different early cancer detection, intraoperative assessment, and postoperative surveillance. However, histological assessment of oncological specimens has inadvertently focused on cancers originating from sporadic tumorigenesis and the primary tumors themselves. Independently, dormant cancers

without primary tumor proliferation may dominate cancer mortality in comparison to proliferative cancers at primary tumor sites. The majority of solid tumors undergo years or decades of latency, which allows for asymptomatic minimal residual disease to ultimately evolve into local recurrences or recurrent metastases. However, proliferation has remained as a hallmark for cancer possibly due to the difficulty in identifying cancer dormancy from circulating blood, bone marrow, and primary tumors. The peri-tumoral field is relevant to field cancerization before the emergence of the primary tumor, and to cancer dormancy after the resection of the primary tumor, and is thus an ideal site to study both phenomena that have been pursued by separate research communities. Unfortunately, the investigation of this field has been largely restricted to genetic analysis without spatial information afforded by H&E histology. We have attempted an extensive investigation of this field by histochemically identifying common cell phenotypes in an organ of interest (breast). This context, along with millimeter-scale wide-field imaging that representatively samples a large surgical specimen from the primary tumor deep into the peri-tumoral field, allows us to detect field cancerization in the peri-tumoral field. Our high-content histochemical imaging of the peri-tumoral field seems to open up new research frontiers for investigation of local invasion and distant metastasis. Clinically, the magenta-colored field cancerization might extend >2 cm beyond the tumor boundary in regions routinely labeled as “normal” by pathologists, necessitating more detailed study on how it changes geographically at a “margin” and the relevance of this to intraoperative assessment.

In the emerging paradigmatic shift in histology from conventional H&E and IHC to SF-vH&E, our imaging platform fills the critical gap to realize slide-free virtual IHC (SF-vIHC) complementary with SF-vH&E. One highly ideal tandem is to perform SF-vH&E by SRS [4] followed by SF-vIHC with our programmable multiphoton imaging, using one robust fiber laser-based optical source suitable for portable application and clinical translation. This tandem, in comparison to an alternative tandem that conducts light-sheet SF-vH&E microscopy [2] followed by the tissue-clearing-assisted volumetric IHC [10], would gain advantage in *in vivo* applications without the tissue clearing and unexpected labeling-induced artifacts, at the moderate cost of lowered imaging speed. The optical source for perspective implementation of this tandem will likely favor our fiber laser-induced supercontinuum over the dedicated fiber laser optimized for SRS [4]. The flexibility in our supercontinuum source to arbitrarily program the excitation pulses (wavelength, bandwidth, chirp, intensity, etc.) has been demonstrated in the first part (Part I) of this study [15], allowing perspective incorporation of coherent Raman scattering microscopy (including SRS). The resulting slide-free virtual histochemistry will advance rapid diagnosis of small biopsies, real-time intraoperative assessment of the surgical tumor margin with plausible field cancerization, imaging-based stratification of cancer patients at an early-stage for precision medicine, and accurate postoperative prognosis or surveillance of minimal residual disease with possible cancer dormancy.

### Funding

National Cancer Institute (R01CA166309 and R01CA213149); National Institute of Biomedical Imaging and Bioengineering (R01EB023232) of the National Institutes of Health.

### Acknowledgment

We thank Darold Spillman for his general technical support and Marina Marjanovic for securing human tissue specimens and obtaining relevant pathological reports.

We thank Anna Higham, Kimberly Cradock, Natasha Luckey, and Z. George Liu from Carle Foundation Hospital for assisting in the acquisition and histological assessment of the human tissue specimens in this study. We also thank the Carle Research Office for assisting in the coordination and consenting in this human subjects research.

## Disclosures

S.A.B., H.T., and S.Y. are named inventors on patents filed by the University of Illinois at Urbana-Champaign related to the development of slide-free virtual histochemistry. All other authors declare that they have no competing financial interests.

S.A.B. and H.T. are co-founders and hold equity in LiveBx, LLC, which is commercializing laser source and imaging technology for slide-free stain-free histopathology.

## References

1. F. Fereidouni, Z. T. Harmany, M. Tian, A. Todd, J. A. Kintner, J. D. McPherson, A. D. Borowsky, J. Bishop, M. Lechpammer, S. G. Demos, and R. Levenson, "Microscopy with ultraviolet surface excitation for rapid slide-free histology," *Nat. Biomed. Eng.* **1**(12), 957–966 (2017).
2. A. K. Glaser, N. P. Reder, Y. Chen, E. F. McCarty, C. Yin, L. Wei, Y. Wang, L. D. True, and J. T. C. Liu, "Light-sheet microscopy for slide-free non-destructive pathology of large clinical specimens," *Nat. Biomed. Eng.* **1**, 0084 (2017).
3. Y. K. Tao, D. Shen, Y. Sheikine, O. O. Ahsen, H. H. Wang, D. B. Schmolze, N. B. Johnson, J. S. Brooker, A. E. Cable, J. L. Connolly, and J. G. Fujimoto, "Assessment of breast pathologies using nonlinear microscopy," *Proc. Natl. Acad. Sci. U.S.A.* **111**(43), 15304–15309 (2014).
4. D. A. Orringer, B. Pandian, Y. S. Niknafs, T. C. Hollon, J. Boyle, S. Lewis, M. Garrard, S. L. Hervey-Jumper, H. J. L. Garton, C. O. Maher, J. A. Heth, O. Sagher, D. A. Wilkinson, M. Snuderl, S. Venneti, S. H. Ramkissoon, K. A. McFadden, A. Fisher-Hubbard, A. P. Lieberman, T. D. Johnson, X. S. Xie, J. K. Trautman, C. W. Freudiger, and S. Camelo-Piragua, "Rapid intraoperative histology of unprocessed surgical specimens via fibre-laser-based stimulated Raman scattering microscopy," *Nat. Biomed. Eng.* **1**, 0027 (2017).
5. T. T. W. Wong, R. Zhang, P. Hai, C. Zhang, M. A. Pleitez, R. L. Aft, D. V. Novack, and L. V. Wang, "Fast label-free multilayered histology-like imaging of human breast cancer by photoacoustic microscopy," *Sci. Adv.* **3**, e1602168 (2017).
6. O. Assayag, M. Antoine, B. Sigal-Zafrani, M. Riben, F. Harms, A. Burcheri, K. Grieve, E. Dalimier, B. Le Conte de Poly, and C. Boccaro, "Large field, high resolution full-field optical coherence tomography: a pre-clinical study of human breast tissue and cancer assessment," *Technol. Cancer Res. Treat.* **13**, 455–468 (2014).
7. N. Roberts, D. Magee, Y. Song, K. Brabazon, M. Shires, D. Crellin, N. M. Orsi, R. Quirke, P. Quirke, and D. Treanor, "Toward routine use of 3D histopathology as a research tool," *Am. J. Pathol.* **180**(5), 1835–1842 (2012).
8. S. R. Kantelhardt, D. Kalasauskas, K. König, E. Kim, M. Weinigel, A. Uchugonova, and A. Giese, "In vivo multiphoton tomography and fluorescence lifetime imaging of human brain tumor tissue," *J. Neurooncol.* **127**(3), 473–482 (2016).
9. D. A. Orringer and S. Camelo-Piragua, "Fast and slide-free imaging," *Nat. Biomed. Eng.* **1**(12), 926–928 (2017).
10. N. Tanaka, S. Kanatani, R. Tomer, C. Sahlgren, P. Kronqvist, D. Kaczynska, L. Louhivuori, L. Kis, C. Lindh, P. Mitura, A. Stepulak, S. Corvigno, J. Hartman, P. Micke, A. Mezheyeuski, C. Strell, J. W. Carlson, C. F. Moro, H. Dahlstrand, A. Östman, K. Matsumoto, P. Wiklund, M. Oya, A. Miyakawa, K. Deisseroth, and P. Uhlén, "Whole-tissue biopsy phenotyping of three-dimensional tumours reveals patterns of cancer heterogeneity," *Nat. Biomed. Eng.* **1**(10), 796–806 (2017).
11. D. P. Slaughter, H. W. Southwick, and W. Smejkal, "Field cancerization in oral stratified squamous epithelium; clinical implications of multicentric origin," *Cancer* **6**(5), 963–968 (1953).
12. B. J. Braakhuis, M. P. Tabor, J. A. Kummer, C. R. Leemans, and R. H. Brakenhoff, "A genetic explanation of Slaughter's concept of field cancerization: evidence and clinical implications," *Cancer Res.* **63**(8), 1727–1730 (2003).
13. G. D. Dakubo, J. P. Jakupciak, M. A. Birch-Machin, and R. L. Parr, "Clinical implications and utility of field cancerization," *Cancer Cell Int.* **7**(1), 2 (2007).
14. K. Curtius, N. A. Wright, and T. A. Graham, "An evolutionary perspective on field cancerization," *Nat. Rev. Cancer* **18**(1), 19–32 (2017).
15. S. You, Y. Sun, E. J. Chaney, Y. Zhao, J. Chen, S. A. Boppart, and H. Tu, "Slide-free virtual histochemistry (Part I): Development via nonlinear optics," *Biomed. Opt. Express* **9**, 5240–5252 (2018).
16. R. He, Y. Xu, L. Zhang, S. Ma, X. Wang, D. Ye, and M. Ji, "Dual-phase stimulated Raman scattering microscopy for real-time two-color imaging," *Optica* **4**(1), 44–47 (2017).
17. G. Deng, Y. Lu, G. Zlotnikov, A. D. Thor, and H. S. Smith, "Loss of heterozygosity in normal tissue adjacent to breast carcinomas," *Science* **274**(5295), 2057–2059 (1996).
18. J. M. Szulczewski, D. R. Inman, D. Entenberg, S. M. Ponik, J. Aguirre-Ghiso, J. Castracane, J. Condeelis, K. W. Eliceiri, and P. J. Keely, "In vivo visualization of stromal macrophages via label-free FLIM-based metabolite imaging," *Sci. Rep.* **6**(1), 25086 (2016).
19. A. J. Ewald, A. Brenot, M. Duong, B. S. Chan, and Z. Werb, "Collective epithelial migration and cell rearrangements drive mammary branching morphogenesis," *Dev. Cell* **14**(4), 570–581 (2008).
20. B. Weigelt, J. L. Peterse, and L. J. van 't Veer, "Breast cancer metastasis: markers and models," *Nat. Rev. Cancer* **5**(8), 591–602 (2005).

21. K. L. Harper, M. S. Sosa, D. Entenberg, H. Hosseini, J. F. Cheung, R. Nobre, A. Avivar-Valderas, C. Nagi, N. Girmius, R. J. Davis, E. F. Farias, J. Condeelis, C. A. Klein, and J. A. Aguirre-Ghiso, "Mechanism of early dissemination and metastasis in Her2<sup>+</sup> mammary cancer," *Nature* **540**(7634), 588–592 (2016).
22. J. A. Aguirre-Ghiso, "Models, mechanisms and clinical evidence for cancer dormancy," *Nat. Rev. Cancer* **7**(11), 834–846 (2007).
23. H. Hosseini, M. M. S. Obradović, M. Hoffmann, K. L. Harper, M. S. Sosa, M. Werner-Klein, L. K. Nanduri, C. Werno, C. Ehrl, M. Maneck, N. Patwary, G. Haunschild, M. Gužvić, C. Reimelt, M. Grauvogl, N. Eichner, F. Weber, A. D. Hartkopf, F.-A. Taran, S. Y. Brucker, T. Fehm, B. Rack, S. Buchholz, R. Spang, G. Meister, J. A. Aguirre-Ghiso, and C. A. Klein, "Early dissemination seeds metastasis in breast cancer," *Nature* **540**(7634), 552–558 (2016).
24. B. K. Wright, L. M. Andrews, M. R. Jones, C. Stringari, M. A. Digman, and E. Gratton, "Phasor-FLIM analysis of NADH distribution and localization in the nucleus of live progenitor myoblast cells," *Microsc. Res. Tech.* **75**(12), 1717–1722 (2012).
25. W. A. Woodward, M. S. Chen, F. Behbod, and J. M. Rosen, "On mammary stem cells," *J. Cell Sci.* **118**(16), 3585–3594 (2005).
26. D. A. Lawson, N. R. Bhakta, K. Kessenbrock, K. D. Prummel, Y. Yu, K. Takai, A. Zhou, H. Eyob, S. Balakrishnan, C.-Y. Wang, P. Yaswen, A. Goga, and Z. Werb, "Single-cell analysis reveals a stem-cell program in human metastatic breast cancer cells," *Nature* **526**(7571), 131–135 (2015).
27. R. Rouzier, C. M. Perou, W. F. Symmans, N. Ibrahim, M. Cristofanilli, K. Anderson, K. R. Hess, J. Stec, M. Ayers, P. Wagner, P. Morandi, C. Fan, I. Rabiul, J. S. Ross, G. N. Hortobagyi, and L. Pusztai, "Breast cancer molecular subtypes respond differently to preoperative chemotherapy," *Clin. Cancer Res.* **11**(16), 5678–5685 (2005).
28. M. Kamei, W. B. Saunders, K. J. Bayless, L. Dye, G. E. Davis, and B. M. Weinstein, "Endothelial tubes assemble from intracellular vacuoles *in vivo*," *Nature* **442**(7101), 453–456 (2006).